Multi-Material 3D Printing of Metamaterials with Targeted Frequency Response

Darshil M. Shah[1], Eric J. Viscione[1], Joshua P. Morris[1], Thomas A. Plaisted[2], Alireza V. Amirkhizi[1], and Christopher. J. Hansen[1,*]

[1]*Mechanical Engineering, University of Massachusetts Lowell, Lowell, MA 01854*
[2]*CCDC Army Research Laboratory, Aberdeen Proving Ground, MD, USA*
[*]Christoper_Hansen@uml.edu

Abstract

Metamaterials possess unconventional mechanical properties that derive from a combination of complex design and tailored material properties. While 3D printing has enabled the fabrication of complex geometries, further performance can be unlocked by multi-material fabrication of geometries with heterogeneous properties. Here, we demonstrate multi-material Digital Light Processing (DLP)-based 3D printing of neat and filled materials with viscosities differing by 3 orders of magnitude. A print method was developed to fabricate complex geometries with intricate features using highly divergent materials requiring different print parameters – including a highly filled (50 vol%) low-density syntactic foam and a neat acrylate resin – with minimal cross-contamination. A metamaterial structure is fabricated using predicted optimal parameters for a 38 kHz frequency response. The print is characterized for its dimensional fidelity and filler cross-contamination. The overall frequency response of the metamaterial structure is compared to its theoretical frequency response. This work further demonstrates its ability to fabricate functional multi-material structures using resins with a broad range of material properties.

Keywords: Multi-material, Digital light processing, Metamaterials, Highly filled materials, 3D printing

1 Introduction

Advances in materials for additive manufacturing (AM) have dramatically expanded the range of material elasticities, from soft hydrogels in the kilopascal (kPa) range to high-strength metals in the gigapascal (GPa) range [1,2]. Extensive studies in filled resin systems have enabled the expansion of material densities, from low density (< 0.85 g cm^{-3}) to high density (> 1.5 g cm^{-3} [3–6]. However, AM techniques limited to a single material cannot fully exploit this diverse range of material properties within a single structure. Topological variation or processing-sensitive chemistries have been pursued to achieve more than a single elasticity, density, and other material properties in a structure, yet they achieve only a fraction of the available property range and at the cost of increased complexity.

The emergence of multi-material AM aims to free the design of functional parts from these restrictions imposed by single-material printing. By enabling the integration of multiple materials with distinct mechanical characteristics into a single structure, multi-material AM opens up new design possibilities that incorporate a wide range of material elasticities, densities, and other properties into a single structure. Multi-material designs have started to be explored for multifunctional applications, such as structures with negative Poisson's ratio [7, 8], tunable thermal expansion [9, 10], gradients in mechanical properties [11], and other applications [12, 13].

Mechanical metamaterials have a unique ability to control wave propagation through their intricate internal structure. They exhibit significant enhancements in the frequency band gap width and design freedom in simulations that introduce multi-material structures [8, 14–16]. Recent review articles on acoustic or ultrasonic metamaterials identify key research thrusts to further propel the technology [17–19].

The integration of metamaterials into applications requires an order-of-magnitude reduction in both size and weight. While alternate designs can enable these reductions in size and weight, material innovation can help achieve further reduction. Smaller periodicity to wavelength ratios enhances the ability to replace the heterogeneous material qualities with a homogenized equivalent system. Systems that can be homogenized with reliable substitute properties can be more easily applied in FEM and complex design applications without adding the tremendous computational cost of a fine microstructure.

A second challenge is the fabrication of micron-scale metamaterial structures with intricate geometries and stringent tolerances. Advanced fabrication methods, particularly additive manufacturing, are perceived as viable solutions for transitioning from small-scale prototypes to scalable, mass-produced panels. As such, emerging metamaterial designs must consider scalability and manufacturing costs to foster wide-scale adoption.

A third thrust seeks metamaterials with dynamic responses applicable across a broadband frequency range. Many cell designs function well at one target frequency but lack absorption at other frequencies. The demand is high for metamaterials capable of covering the entire acoustic range, with wider absorption and stop bands without an increase in overall material thickness. Multi-material printing can address each of these three thrusts.

Multi-material printing has been demonstrated in numerous 3D printing techniques, including fused filament fabrication (FFF) [20–23], direct ink writing (DIW) [24], polyjet [12], and selective laser sintering (SLS) [25].

However, each is limited in the production of the next generation of metamaterial designs. In FFF, the resolution is relatively low, and material choice is limited to those suitable for filament dispensing [26]. DIW also suffers from low resolution issues. The multi-material DIW processes also tend to be slow since each layer is created by tracing out 1D lines [27]. Polyjet requires specific viscosity and temperature needs for jetting, limiting the material selection [28]. SLS printing technique has limited polymeric material choice, difficulty to achieve prints with multiple materials in a single layer, and contamination concerns between different powders [29, 30].

Vat-based polymerization methods - such as stereolithography (SLA) and digital light processing (DLP) - offer both high resolution, diverse material feedstocks, and potential for scalable production. Early multi-material SLA-based approach required time-consuming and geometry-limiting manual vat exchanges and cleaning the parts of residual resin between material changes [31]. Subsequent attempts streamlined the printing process for designs in which one material is fabricated before switching to another material [32–34].

The manual changing of vats was addressed by a rotating carousel system, while the cleaning was replaced with an automatic ultrasonic solvent bath and physical cleaning [28]. The cleaning procedure, at 3 min per layer, made it difficult to print geometries of large numbers of layers. Solvent cleaning increases the risk of solvent trapped in the fabricated part adversely impacting its mechanical properties. Finer features (300 μm) were also damaged during the cleaning process [28, 34]. Wang et al. used a rotating wheel to deliver the resin in droplet form to print structures. Metamaterial structures with negative coefficients of thermal expansion (CTE) were fabricated using poly(ethylene glycol di-acrylate) (PEGDA) along with PEGDA filled with 10 vol% copper. Despite its success, the process was time-consuming, taking over 6 hours to print 6 mm height structure with observed filler contamination [35].

Multi-material lattice structures have been fabricated by cleaning excess resin from the structures using high-pressure air-jet [36]. A similar multi-material lattice geometry was fabricated with negative Poisson's ratio functionality [8]. While these approaches reduced the resin contamination, they were well suited to lower viscosity resins and to structures with low cross-sectional surface area, such as open lattices. Higher viscosity-filled resin systems with closed geometries can be difficult to fabricate with only air jets as the sole cleaning mechanism.

Multi-material, high resolution structures were fabricated with high viscosity filled resins using a dynamic fluid exchange process [37]. The process involves purging the resin to replace it with the second resin system to achieve multi-material capabilities. The entailed wasted resin limits the multi-material geometries to be less than 2 mm. Scaling up the process is also difficult due to high material wastage, increased print times due to purging, and the costs involved.

A recent resin multi-material 3D printing approach, based on the continuous liquid interface production (CLIP) method, is called injection CLIP (iCLIP) [38]. The iCLIP method relies on injecting the resin through microfluidic conduits or viaducts within the part. Utilizing viaducts to transport resin significantly speeds the multi-material printing process by reducing the suction forces and eliminating the need for resin re-flow. The viaducts also enable printing with high-viscosity resin systems, albeit with constrained size and time limitations due to suspension instabilities. The design of any desired multi-material structures, however, revolves around the presence of these viaducts proving detrimental to its mechanical properties, unless, however, the viaducts are refilled with the resin and cured in the post-processing step. Complex geometries with relatively high surface area also require multiple viaducts in the geometry. Print resolution is adversely affected for the features around the viaducts, thereby limiting fabrication of parts with intricate features, a core requirement for metamaterials.

The existing body of work in multi-material SLA/DLP requires developing an expensive printer from ground-up with complex systems to automate the material exchange and cleaning process. Despite which, fabricating larger geometries (>10 mm), with high surface area and closed design, with highly filled (>35 vol%) resin, without significant filler contamination, remains a challenge.

Here, a multi-material DLP (MM-DLP) printer capable of fabricating highly filled material systems is demonstrated at scales suitable to produce mechanical metamaterials with targeted frequency response. By modifying an open-source printer to include an automated material exchange and simple cleaning mechanism, a 50 vol% filled low density (0.81 g cm^{-3}) syntactic foam and a relatively high density (1.215 g cm^{-3}) neat acrylate resin are used as a demonstration. A complex multi-material, metamaterial geometry with density contrast achieving enhanced targeted frequency transmission response [14] is fabricated as an exemplar. The frequency response of the fabricated multi-material metamaterial structure is compared against the theoretical response further demonstrating the overall print functionality and fidelity.

2 Materials and Methods

2.1 Materials

The formulations from this study were based on the commercially available, open-source resin PR48 developed by Autodesk [39, 40]. A low density, highly filled resin –named MF-HG –was prepared based on the formulation given in [41]. The monofunctional reactive diluent 2-[[(Butyl-amino)-carbonyl]oxy]ethyl acrylate (Genomer 1122) was obtained from Rahn AG, USA. The multifunctional monomer ethoxylated pentaerythritol tetraacrylate (Sartomer SR494) was purchased from Arkema (USA). The photoinitiator diphenyl (2,4,6-trimethyl-benzoyl)phosphine oxide (TPO) was purchased from Frontier Scientific (USA). The UV absorber 2,5-Bis(5-tert-butyl-benzoxazol-2-yl)thiophene (TBT) was purchased from Sigma Aldrich (USA). Low-density, hollow glass microspheres (K42HS) were provided by 3M, USA. The dispersant BYK w980 was obtained from BYK Additives and Instruments (USA). All materials were used as received.

2.2 Multi-material printer

The MM-DLP system was created by modifying an Autodesk Ember printer to enable multi-material capabilities. Positional tracking of the resin vat was achieved using Hall effect sensors (KY-003, Fritzing) and conformable magnets (McMaster-Carr). A peristaltic fixed-flow-rate metering pump (McMaster-Carr) dispensed the resin. Cleaning and uniform coverage of the resin on the print window were achieved with a pressurized air system, which features a 5-position air manifold (Primefit) with electronically actuated solenoid (AOMAG) to individually control airflow to each air jet. Between printing each layer, the build head compresses into a soft urethane foam pad (Morning Glory) to remove excess resin. The vat containing MF-HG resin was fitted with a 0.2 optical density (OD) neutral density filter

(Edmund Optics) to reduce the transmission of incident UV light by 40%. The control and communication of system components were managed with an Arduino Mega 2560 (Arduino) programmed using the Arduino framework based on C++.

2.3 Post-fabrication of multi-material structures

The residual resin was removed from the fabricated specimen by submerging it in Isopropyl Alcohol (IPA, Fisher Scientific, USA) and ultrasonicating it for 10 minutes. The prints were then gently dried with compressed air. Subsequently, the specimen was transferred to a custom nitrogen-filled borosilicate glass enclosure. The enclosure was placed in a Form Cure device (Formlabs, USA) for a 2-hour post-curing process. The exposure intensity was 6.5 mW cm^{-2} at 405 nm.

2.4 Thermogravimetric analysis (TGA) of filler content

The filler content within the head feature of the metamaterial was determined by thermogravimetric analysis (TGA) using a Discovery TGA (TA Instruments, USA). TGA measurements were conducted on both the MF-HG walls and the PR48 head at three locations: the initial layers (closest to the build head), the middle layers (at the approximate center of the structure), and the final layers of the printed structure. The specimen was sectioned to obtain specimens weighing between 16–20 mg. The specimen was heated from room temperature to 700 °C at a ramp rate of 20 °C min-1 under a nitrogen environment.

2.5 Microscope imaging

Images of individual unit cells were taken using a stereo microscope (Zeiss Discovery V20) for dimensional analysis. The images were then processed with MATLAB using a custom code.

2.6 Density measurement

The density of the fabricated specimen was calculated based on Archimedes' principle. The measurements were collected using a Sartorius density measurement kit (YDK01, Cole-Parmer, USA) and a balance (Sartorius Practum313-1S, Cole Parmer, USA). Ethyl alcohol (Fisher Scientific, USA)) was used as the suspending medium. The balance has a precision of 0.001 g.

2.7 Characterization of metamaterial performance

The transmission performance of the printed metamaterial specimens was characterized using a transmission bar experiment. The specimens were placed between two long aluminum bars. A transducer excited the end of one aluminum bar, using a sinusoidal signal progressively stepped from 24 to 50 kHz at 100 Hz intervals. The signal is measured using semiconductor strain gages located 20 and 30 mm from the ends of the bars in contact with the specimen. The amplitude and phase measurements were used to construct the transfer matrix for the sample, from which the scattering coefficients and apparent properties were extracted [42]. Comparison and validation of the measured results were conducted using predictions from 2D scattering FEM. The modeling and experiment method and analysis followed the Long Cycle approach detailed in [43].

3 Results and Discussion

3.1 Multi-Material AM Process

We introduce multi-material print capabilities by modifying an open-source, DLP-based 3D printer. The DLP printer, the Autodesk Ember, utilizes a sequential process to transform a digital design into a physical object fabricated from a single material. A digital micromirror device (DMD) reflects a 405 nm UV light source to generate 2D images. The light is transmitted through a Polydimethylsiloxane (PDMS) window into a vat, where a layer of the liquid photopolymer resin is cured and attaches to a build head situated directly above the window. Following photocuring, the vat rotates by 60° while the build head raises by a user-defined z-axis layer height to separate the printed layer from the window and to allow for resin re-flow. The resin vat returns to the initial position for curing the subsequent layer. This process repeats until all layers are fully cured, resulting in a 3D object. The printer offers a resolution of 50 μm in the $x - y$ plane and accommodates a z-axis layer thickness between $10 - 100$ μm [39].

We modify this process via alterations to the printer and its source code to print multi-material parts. Whereas the vat rotated back and forth by 60° to print with a single material, the code was modified [44]to progressively rotate through 360° to interact with multiple vats containing different resin materials. A schematic of the vat positions and accompanying modifications are shown in Figure 1.

The resin material was dispensed as needed via a dispenser per material, rather than the vat containing a bath of material. In multi-material printing, the resin viscosities are often distinct; the direct dispensing approach ensures a more controllable flow to cover the exposure window. A low-pressure air jet (35 psi) is directed at the window and spreads the resin uniformly over the window. Compared to the conventional resin-filled vat, the resin dispensing approach also minimizes the need to clean leftover resin after curing each layer.

To accommodate the resin's different cure characteristics and prevent over-exposure of a resin material [41,45], an optical density (OD) neutral density filter is installed. For this work, the vat dedicated to the MF-HG resin contains a 0.2 optical density filter to reduce the UV light intensity by 40%.

Even with the reduced excess resin exposure due to precise material dispensing, contamination between vats can occur without intervention. We introduce a physical cleaning mechanism between each material change in the printing cycle. Two urethane foam pads are placed between the windows on each resin vat, which absorb excess liquid resin after a layer has been printed and provide additional cleaning via shearing action during layer separation. A second, high-pressure air jet (100 psi), removes excess, potentially contaminated liquid resin from the window, preparing it for a fresh layer of resin to be dispensed.

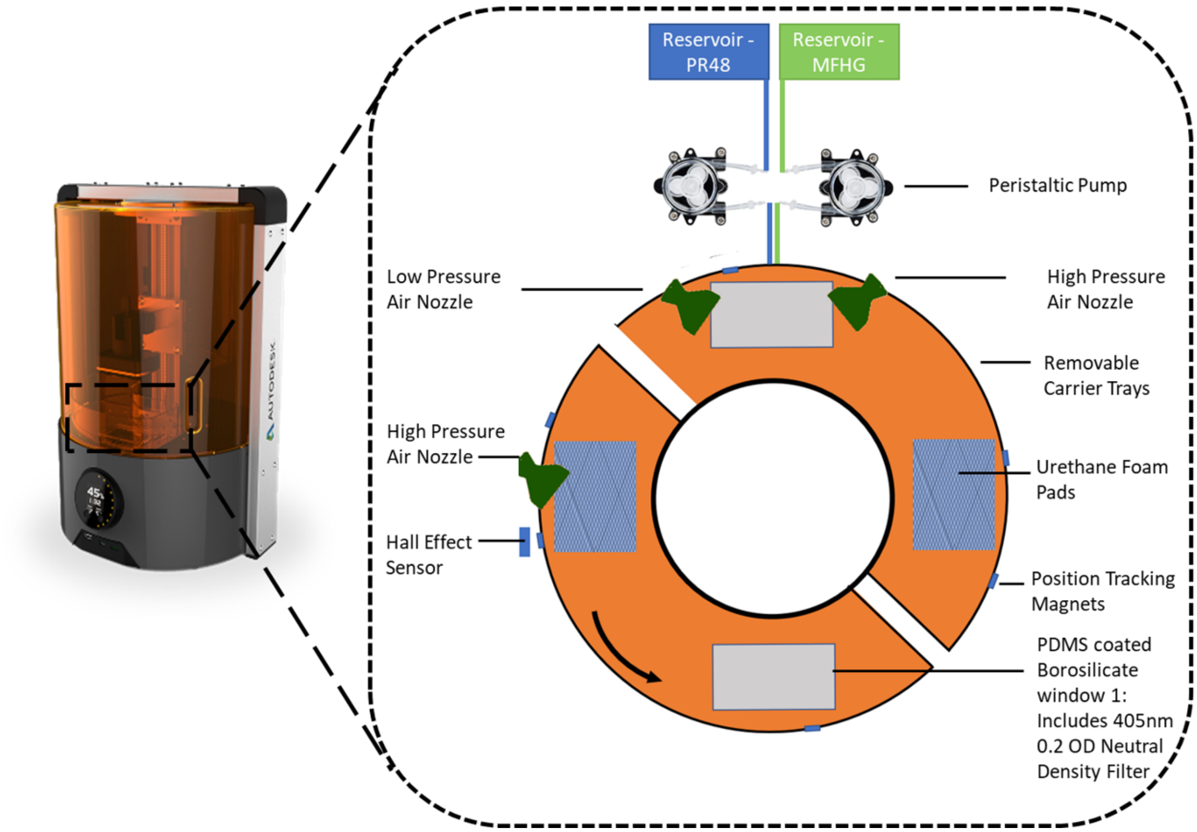

Figure 1: Schematic of the multi-material specific components for the MM-DLP printer.

A complete print cycle is illustrated in Figure 2a. The cycle starts with the window for Material A in position for photocuring (step 1). While Material A is exposed, Material B is dispensed onto the second window and spread with the low-pressure air jet.

The vat then rotates by 30°, and the build head ascends to separate the printed layer from the window (step 2). The vat rotates by a further 60°, positioning the build head directly above a foam block (step 3). The build head descends into the foam block, effectively clearing off excess resin and maintaining the set z-axis layer height.

Next, the vat rotates by an additional 90°, reaching a position where Material B has been pre-dispensed (step 4). During the rotation phase, high-pressure air jets are activated, eliminating excess resin of Material A from the window and foam block. Following the 90° rotation, the build head descends to a predetermined height, leaving a gap to print the required layer height from Material B. The cycle then continues with the positions of Material A and Material B being swapped.

The printer compensates for layer height each time the build head descends. This approach results in an effective layer height that is double the user-defined z-axis layer height due to two descents within each cycle. The vertical positions of the final printed material are shown in Figure 2b.

3.2 Multi-material metamaterial printing using MM-DLP

The target metamaterial geometry is shown in Figure 3a where the features to be printed with MF-HG are shown in green, and the features printed with PR48 are shown in blue. The 3D model is split into two different features; the frame and the resonator head to be printed with the MF-HG, and PR48, respectively as shown in Figure 3b. The MF-HG frame has an overlap of 0.15 mm with the PR48 resonator head. This overlap accounts for 2.67 % of the PR48 resonator head volume. These individual 3D features are then sliced in the Print Studio software generating a series of images of these individual features. The images are then extracted and stacked along with blank images to account for the cleaning process between two layers using a custom MATLAB script. Figure 3c shows the printed multi-material metamaterial specimen. The overall print time is around 5.5 hours.

For the first time, a 20 mm long, multi-material part was fabricated with a highly filled (50 vol%) resin and a neat resin. The hollow channels are resolved completely as observed in Figure 3c (i). The flat surface as observed in Figure 3c(ii) is rough due to the presence of 50 vol% of hollow glass fillers, that can, however, be sanded off for cosmetic purposes.

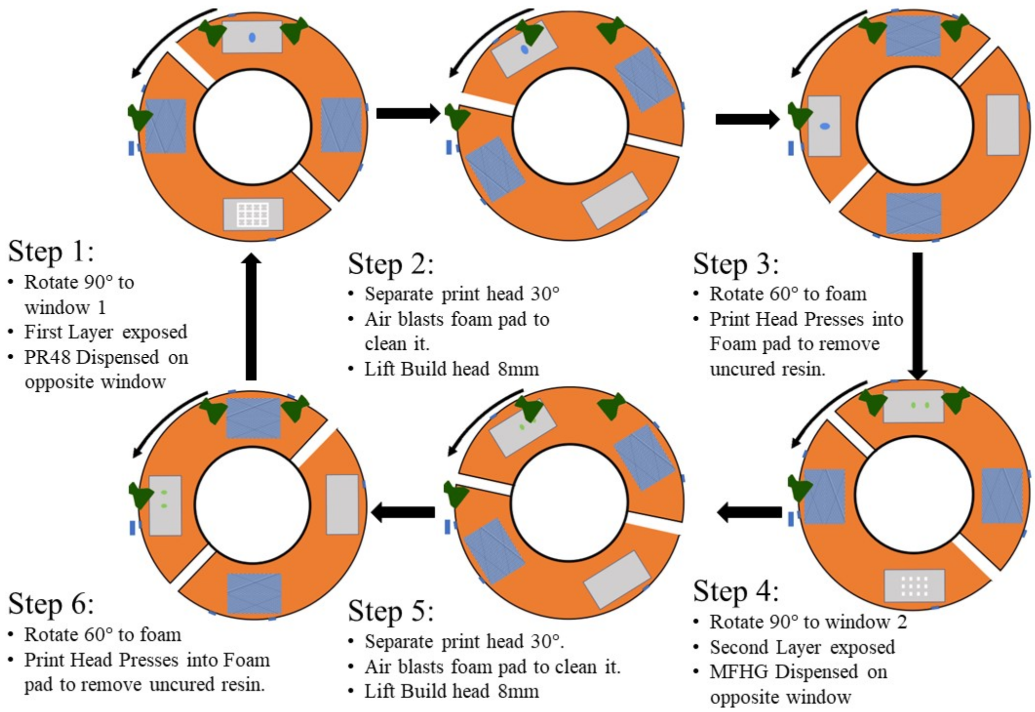

(a)

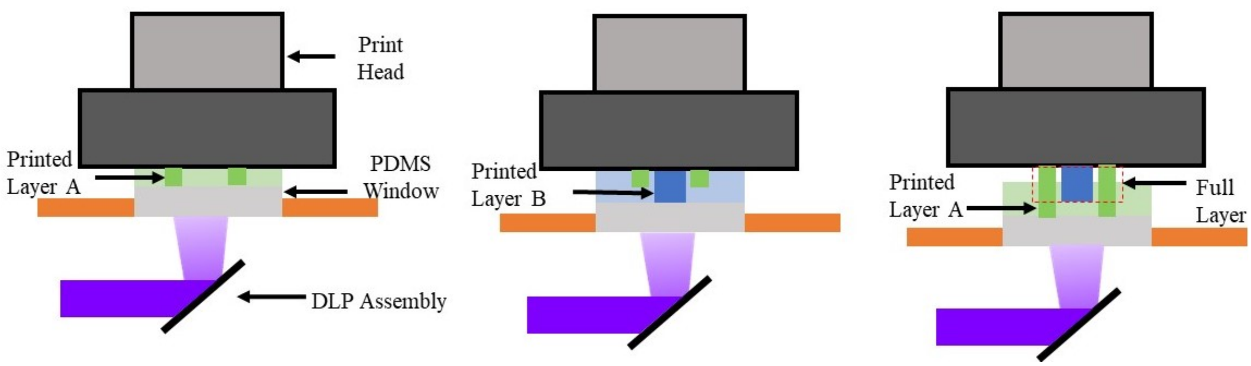

(b)

Figure 2: a) Schematics of the print cycle and b) layer stacking of the MM-DLP.

3.3 Dimensional Analysis

Metamaterial performance is sensitive to the dimensional fidelity of the unit cell [43]. The fabricated multi-material metamaterial specimen was subsequently imaged and characterized for its dimensions. Figure 4a shows an optical microscope image of one of the unit cells used for dimensional analysis using MATLAB. A custom script was used to automate the interested feature identification of the unit cell eliminating user bias. Figure 4b features an annotated version of the unit cell labeling each dimension recorded in a unit cell. Target

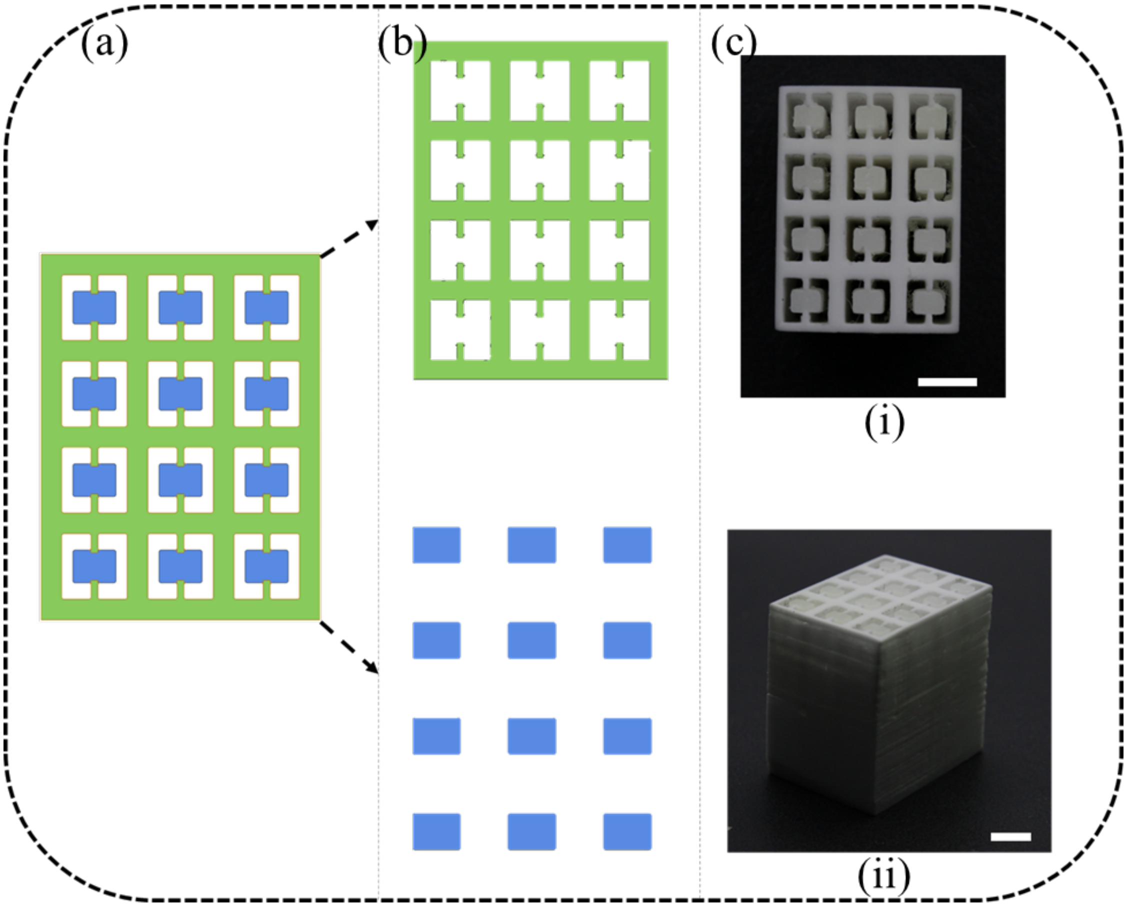

Figure 3: a) Target metamaterial geometry shape, b) split into two separate features to be printed with two different materials, and c) multi-material fabricated metamaterial specimen (all scale bar 5 mm).

dimensions and measured average dimensions of highlighted features in Figure 4b for all the 12 unit cells are reported in 1.

Target dimensions comprises of positive features with a range of dimensions. The web width being the smallest positive feature with 400 μm is measured to be an average of 451 μm. The increased dimensions is due to the cured width broadening caused by filler presence in the web feature. The head width and head height features report shrinkage due to the curing of the neat resin, a common feature of an unfilled resin [46]. Most of the features report dimensional error well under 10 %, with an exception of web width where the error is reported at 12.8 %. However, the absolute difference is only 51 μm, which is close to the

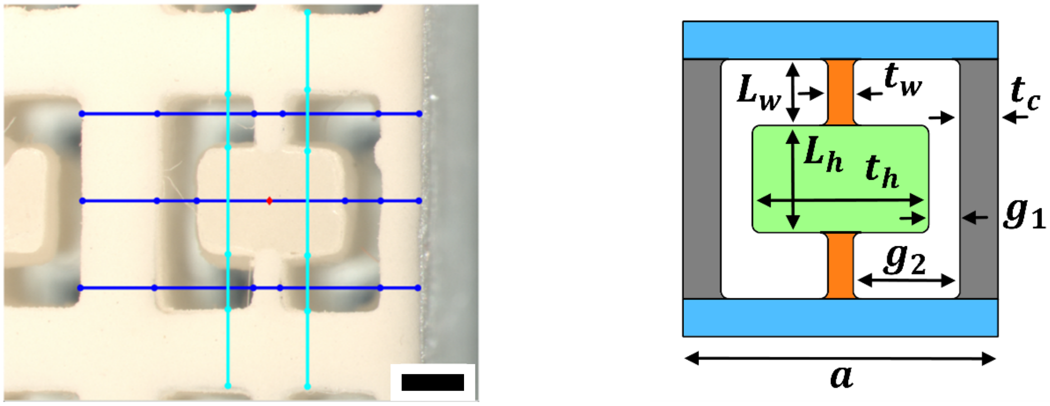

(a) (b)

Figure 4: a) Optical microscope image of a unit cell of the multi-material metamaterial highlighting dimensions to be measured using MATLAB (scale bar 1 mm). b) Annotated unit cell to identify measured dimensions.

Table 1: Accuracy of the printed multi-material specimen from averaged dimensions of 12 cells.

Feature Description	Target Dimensions (μm)	Measured Dimensions (μm)	Difference (μm)	Error (%)
Web Width, t_w	400	451	51	12.8
Head Width, t_h	2500	2429	-71	-2.8
Head Height, L_h	1900	1729	-171	-9.0
Gap Width, g_1	650	618	-32	-4.9
Gap Width, g_2	1700	1605	-95	-5.6
Web Length, L_w	950	923	-27	-2.9
Walls, t_{cx}	600	623	23	3.9
Walls, t_{cy}	600	638	38	6.3
Cell Width, a_x	5000	4909	-91	-1.8
Cell Width, a_y	5000	4850	-150	-3.0

printer resolution of 50 μm in the $x - y$ plane [39]. Given the divergent nature of the two material systems and the contrasting exposure energy/exposure time as reported by Shah et al. [41], the dimensional accuracy of this multi-material print seems fairly decent.

3.4 Density measurement

The density of the fabricated specimen was measured post-printing using Archimedes' principle and compared with the theoretical density estimates. The experimental density of the fabricated specimen was measured to be 0.937 g cm^{-3}. The theoretical density estimate for the fabricated multi-material part (ρ_{MM})was based on the overall volume for MF-HG (V_{MF-HG}) and PR48 (V_{PR48}) using the dimensions in SolidWorks. The densities reported as 0.81 g cm^{-3} in [41] and 1.215 g cm^{-3} measured experimentally for MF-HG (ρ_{MF-HG})and PR48 (ρ_{PR48})were used respectively. The theoretical density for a part with no voids can be estimated based on a rule of mixtures approach:

$$\rho_{MM} = V_{MF-HG}\rho_{MF-HG} + V_{PR48}\rho_{PR48} \tag{1}$$

Using the reported densities and calculated volumes, the ideal density of the multi-material part is estimated to be 0.938 g cm^{-3}. The calculated and experimentally measured density match closely and differ by 0.1%. This implies that there is no contamination coming from the excess window on the resin. Any potential contamination could be from the cross-contamination of fillers from the features printed with MF-HG to features printed with PR48. TGA analysis could be performed to further evaluate the potential cross-contamination.

3.5 Filler cross-contamination measurement

The overall metamaterial performance in achieving the targeted frequency response is highly dependent on the density contrast achieved by the two resins: low-density MF-HG on the walls and webs, and high-density PR48 on the head. Filler cross-contamination into PR48 is of utmost importance to understand the quality of the multi-material print as well as the final frequency response of the fabricated metamaterial compared with the theoretical prediction. TGA was performed on one of the unit cells for both MF-HG, and PR48 resin at three locations through the print direction, representing the beginning (top), middle, and end (bottom) of the print. Once the specimen is heated above 500 °C, the organic content is decomposed leaving behind char content and the inorganic content (hollow glass fillers). TGA is an approximate, but one of the most direct ways to quantify filler contamination as shown in [4, 41]. Figure 5 shows the mass loss for PR48 and MF-HG as a function of temperature for three above-mentioned locations.

The filler contamination is calculated based on the true density of 0.42 g cm^{-3} for the inorganic hollow glass microsphere and 1.215 g cm^{-3} for the organic PR48 resin. The PR48 head is isolated from the unit cell to be tested in the TGA. However, since the head feature has a slight overlap of the MF-HG web of 2.67 vol% of the entire head volume, an ideally sectioned head has 1.33 vol% of hollow glass fillers present as a baseline.

The residual masses at 700 °C for the top, middle, and bottom layers of PR48 are 6.64 wt%, 5.5 wt%, and 8.01 wt% respectively. The char content for pure PR48 resin is 6.08 $\pm$ 1.77 wt% (6 specimens). The filler contamination is based on these residual weights, char content, and accounting for baseline filler presence, corresponding to approximately 0.38 vol%, -3.12 vol%, and 4.52 vol% at the top, middle, and bottom layers, respectively. The negative contamination for the middle layers is due to the slightly lower residual mass for the middle layers compared to the char content. The volume % value is extremely sensitive to small changes in the weight % due to lower density values for the fillers. Despite the sensitivity, overall filler contamination is within 5 vol% throughout the print, good enough to not significantly affect the metamaterial performance.

Similarly, the residual masses for MHFG walls at 700 °C for the top, middle, and bottom layers are 25.58 wt%, 27.27 wt%, and 25.47 wt% respectively. The char content for the unfilled MF-HG is 3.75 $\pm$ 0.08 wt%. The corresponding filler volume fraction is 46.17 vol%, 48.6 vol%, and 46.01 vol% throughout the resin as compared to the target filler volume fraction of 50 vol%. The variation within the print is 2.59 vol% whereas the overall filler vol% is within 5 vol% of the target vol% thereby validating the resin stability throughout the print.

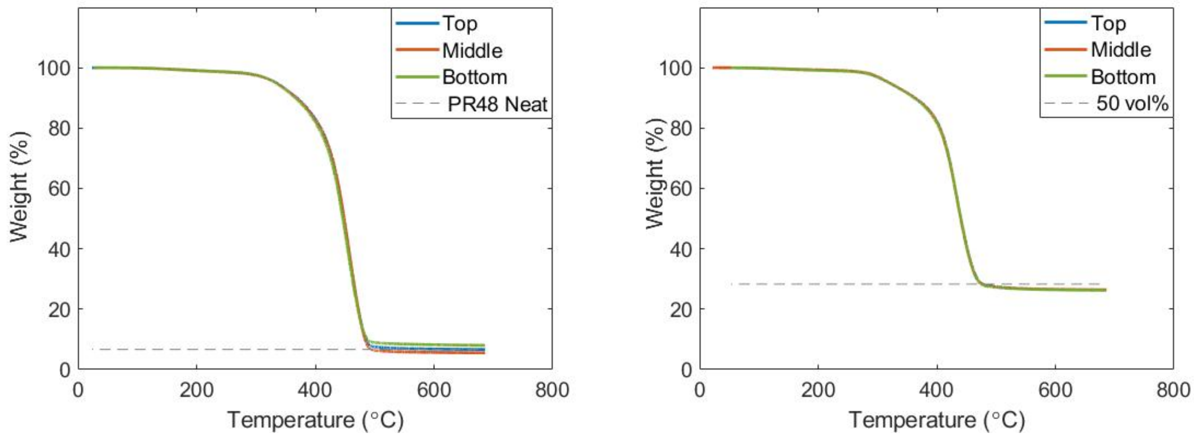

(a) (b)

Figure 5: a) Mass loss for the PR48 head feature compared to the PR48 char content and b) mass loss for the MF-HG walls compared to the 50 vol% ideal mass loss at three different locations through depth.

3.6 Metamaterial Performance

The printed metamaterial is expected to demonstrate stop band behavior, where transmission is attenuated over a designated range of frequency. Figure 6 compares the measured transmission performance to modelled predictions using the measured dimensions from Supplementary Table 1, and 5 vol% contamination between PR48 (5 vol% PR48), and MF-HG (45 vol% MF-HG) . Experiment results confirm the quality of the sample meets the sensitive tolerances for metamaterial fabrication. Around 40 kHz, the magnitude of the transmitted signal drops by two orders of magnitude (compared to a lower frequency) before beginning to increase again as it approaches the transducer's high frequency cut-off. Consistent with the results for the single material PR48 sample in [43], the experiment captures the general shape and stop band location well but misses finer detail. This is due to the resin's inherently high loss and impedance mismatch between bar-sample, not the quality of the print.

Multi-material unit cells enable enhanced attenuation performance by increasing the contrast between the outer frame and inner resonator mass. This results from the decoupling of the two structural (controls transmission outside the stop band) and resonant components (transmission within the stop band). The advantages are clear when comparing the trans-

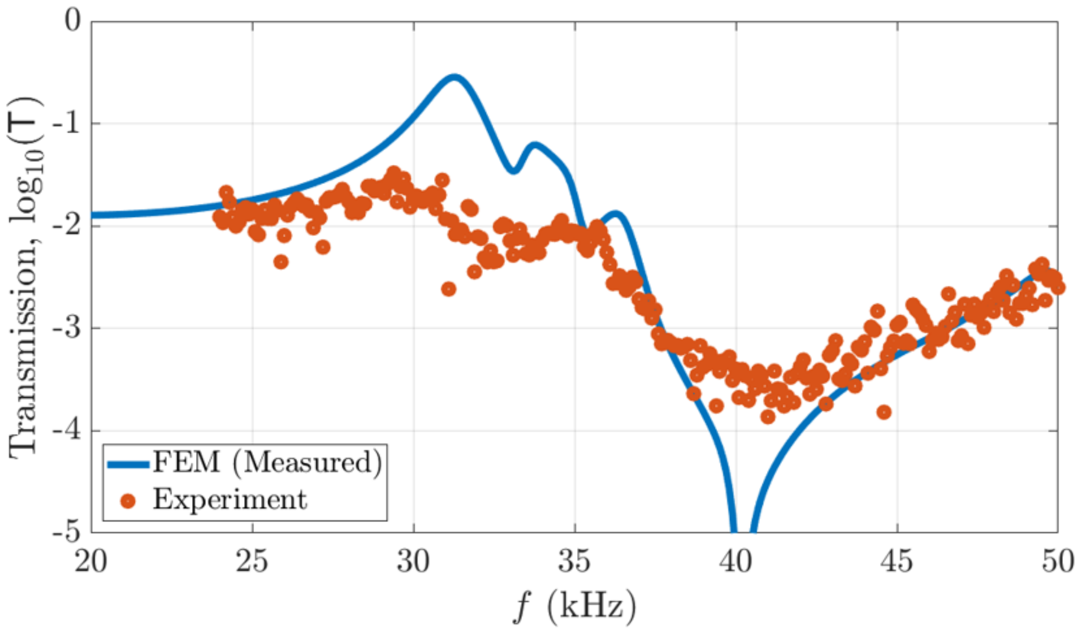

Figure 6: The metamaterial sample demonstrates stop band attenuation and good agreement with modelled transmission predictions.

mission curves for arrays made using a single material (PR48) [43] or multiple materials with contrasting mass (PR48 and MF-HG). As shown in Figure 7, the PR48 and MF-HG cell with the Target Dimensions from Table 1 offers enhanced band depth compared to the single material case with similar bandwidth. However, the optimized version from [14] with better mass contrast provides nearly double the bandwidth of the others.

Advantages are also realized in terms of shape when multiple materials are incorporated into the cell design. The single material cell required a more complex H-shaped inclusion with smaller gaps. This H shape allows for the maximum possible head mass via increases in volume. If instead mass (or mass contrast) is added by changing the head material, a simpler X-shaped inclusion is possible. The simplified X shape is less sensitive to geometric error, is easier to clear excess resin from, and results in fewer print failures.

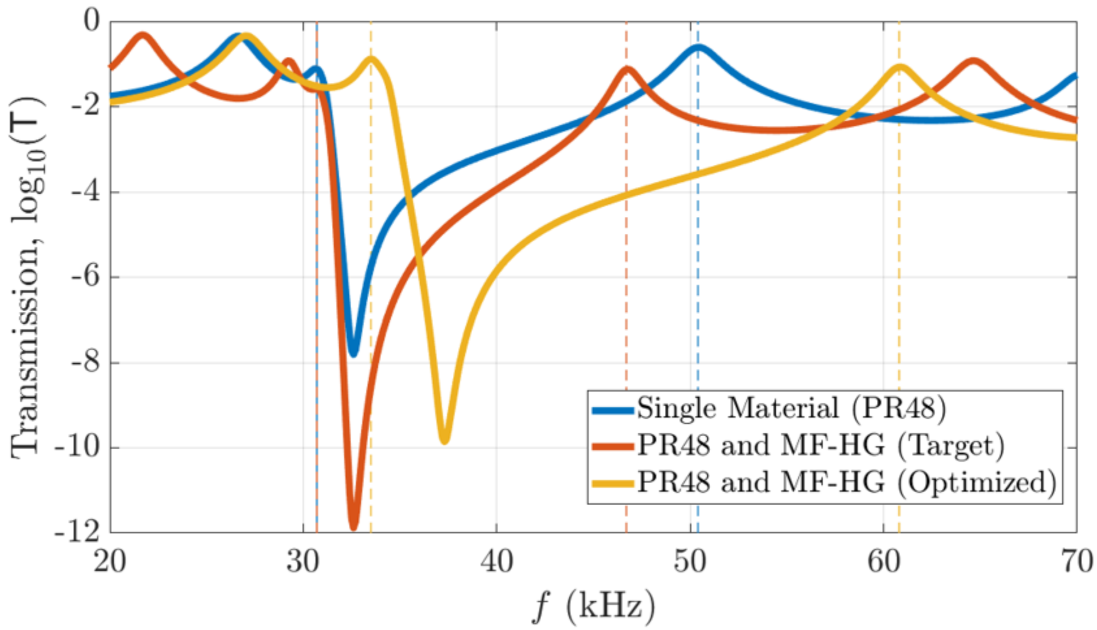

Figure 7: Multi-material printing offers enhanced stop band depth and width compared to single material unit cells. The dashed lines indicate the bounds of each stop band.

4 Conclusion

A commercial low-cost DLP-based Autodesk Ember 3D printer was modified to achieve multi-material printer capabilities. For the first time, a 20 mm long part was fabricated with a highly filled (50 vol%) resin system (MF-HG) along with a neat PR48 resin to demonstrate the multi-material capabilities of the MM-DLP system. The fabricated metamaterial showed relatively robust resin suspension stability over the course of the print. The filler content was observed to be lower by roughly within 5 vol% of the target filler fraction. While a similar range of filler contamination was observed in the neat PR48 resonator head. Given that the print density matched closely with the theoretical density observed, most of the contamination was from the printed layers, rather than from the excess resin on the window. The contamination was still within the metamaterial sensitivity limit where a two-order drop in the transmission signal was observed at the targeted frequency matching well with the theoretical results. A clear advantage of multi-material metamaterial was demonstrated in terms of wider and deeper stop bands. This work guides the development of potential desktop-type multi-material printers with high resolution to print metamaterials with auxetic properties, multi-functional structures, multi-color prints, and a myriad of other applications.

Acknowledgements

This research was supported by CCDEVCOM Army Research Laboratory through Cooperative Agreement W911NF-17-2-0173.

References

[1] J. Borrello, P. Nasser, J. C. Iatridis, and K. D. Costa, "3d printing a mechanically-tunable acrylate resin on a commercial dlp-sla printer," *Additive manufacturing*, vol. 23, pp. 374–380, 2018.

[2] Q. Thijssen, A. Quaak, J. Toombs, E. De Vlieghere, L. Parmentier, H. Taylor, and S. Van Vlierberghe, "Volumetric printing of thiol-ene photo-cross-linkable poly (ε-caprolactone): A tunable material platform serving biomedical applications," *Advanced Materials*, p. 2210136, 2023.

[3] D. M. Shah, *3D Printing of and Light Scattering in Highly Filled Systems for Mechanical Metamaterials*. PhD thesis, University of Massachusetts Lowell, 2023.

[4] T. Roques-Carmes, P. Marchal, A. Gigante, and S. Corbel, "Stereolithography fabrication and characterization of syntactic foams containing hollow glass microspheres," *Russian Chemical Reviews*, vol. 78, no. 4, pp. 375–386, 2009.

[5] M. Layani, X. Wang, and S. Magdassi, "Novel materials for 3d printing by photopolymerization," *Advanced Materials*, vol. 30, no. 41, p. 1706344, 2018.

[6] D. A. Komissarenko, P. S. Sokolov, A. D. Evstigneeva, I. A. Shmeleva, and A. E. Dosovitsky, "Rheological and curing behavior of acrylate-based suspensions for the DLP 3D printing of complex zirconia parts," *Materials*, vol. 11, no. 12, 2018.

[7] X. Kuang, J. Wu, K. Chen, Z. Zhao, Z. Ding, F. Hu, D. Fang, and H. J. Qi, "Grayscale digital light processing 3D printing for highly functionally graded materials," *Science Advances*, vol. 5, no. 5, pp. 1–10, 2019.

[8] D. Chen and X. Zheng, "Multi-material Additive Manufacturing of Metamaterials with Giant, Tailorable Negative Poisson's Ratios," *Scientific Reports*, vol. 8, no. 1, pp. 1–8, 2018.

[9] L. Wu, B. Li, and J. Zhou, "Isotropic negative thermal expansion metamaterials," *ACS applied materials and interfaces*, vol. 8, no. 27, pp. 17721–17727, 2016.

[10] R. Lakes, "Cellular solids with tunable positive or negative thermal expansion of unbounded magnitude," *Applied physics letters*, vol. 90, no. 22, p. 221905, 2007.

[11] R. Libanori, R. M. Erb, A. Reiser, H. Le Ferrand, M. J. Süess, R. Spolenak, and A. R. Studart, "Stretchable heterogeneous composites with extreme mechanical gradients," *Nature communications*, vol. 3, no. 1, pp. 1–9, 2012.

[12] A. Bandyopadhyay and B. Heer, "Additive manufacturing of multi-material structures," *Materials Science and Engineering R: Reports*, vol. 129, no. March, pp. 1–16, 2018.

[13] M. Vaezi, S. Chianrabutra, B. Mellor, and S. Yang, "Multiple material additive manufacturing–Part 1: a review: this review paper covers a decade of research on multiple material additive manufacturing technologies which can produce complex geometry parts with different materials," *Virtual and Physical Prototyping*, vol. 8, no. 1, pp. 19–50, 2013.

[14] J. Morris, W. Wang, D. Shah, T. Plaisted, C. J. Hansen, and A. V. Amirkhizi, "Expanding the design space and optimizing stop bands for mechanical metamaterials," *Materials and Design*, vol. 216, p. 110510, 2022.

[15] S. A. Cummer, J. Christensen, and A. Alù, "Controlling sound with acoustic metamaterials," *Nature Reviews Materials*, vol. 1, no. 3, pp. 1–13, 2016.

[16] G. Liao, C. Luan, Z. Wang, J. Liu, X. Yao, and J. Fu, "Acoustic metamaterials: A review of theories, structures, fabrication approaches, and applications," *Advanced Materials Technologies*, vol. 6, no. 5, p. 2000787, 2021.

[17] S. Chen, Y. Fan, Q. Fu, H. Wu, Y. Jin, J. Zheng, and F. Zhang, "A review of tunable acoustic metamaterials," *Applied Sciences*, vol. 8, no. 9, p. 1480, 2018.

[18] S. Krödel and C. Daraio, "Microlattice metamaterials for tailoring ultrasonic transmission with elastoacoustic hybridization," *Physical Review Applied*, vol. 6, no. 6, p. 064005, 2016.

[19] G. Liao, C. Luan, Z. Wang, J. Liu, X. Yao, and J. Fu, "Acoustic metamaterials: A review of theories, structures, fabrication approaches, and applications," *Advanced Materials Technologies*, vol. 6, no. 5, p. 2000787, 2021.

[20] A. Abilgaziyev, T. Kulzhan, N. Raissov, M. H. Ali, W. L. Match, and N. Mir-Nasiri, "Design and development of multi-nozzle extrusion system for 3D printer," *2015 4th International Conference on Informatics, Electronics and Vision, ICIEV 2015*, pp. 1–5, 2015.

[21] L. R. Lopes, A. F. Silva, and O. S. Carneiro, "Multi-material 3D printing: The relevance of materials affinity on the boundary interface performance," *Additive Manufacturing*, vol. 23, no. March, pp. 45–52, 2018.

[22] D. Espalin, J. A. Ramirez, F. Medina, and R. Wicker, "Multi-material, multi-technology FDM: Exploring build process variations," *Rapid Prototyping Journal*, vol. 20, no. 3, pp. 236–244, 2014.

[23] J. Yin, C. Lu, J. Fu, Y. Huang, and Y. Zheng, "Interfacial bonding during multi-material fused deposition modeling (FDM) process due to inter-molecular diffusion," *Materials and Design*, vol. 150, pp. 104–112, 2018.

[24] M. A. Skylar-Scott, J. Mueller, C. W. Visser, and J. A. Lewis, "Voxelated soft matter via multimaterial multinozzle 3D printing," *Nature*, vol. 575, no. 7782, pp. 330–335, 2019.

[25] H. Sahasrabudhe, R. Harrison, C. Carpenter, and A. Bandyopadhyay, "Stainless steel to titanium bimetallic structure using LENS™," *Additive Manufacturing*, vol. 5, pp. 1–8, 2015.

[26] S. C. Ligon, R. Liska, J. Stampfl, M. Gurr, and R. Mülhaupt, "Polymers for 3D Printing and Customized Additive Manufacturing," *Chemical Reviews*, vol. 117, no. 15, pp. 10212–10290, 2017.

[27] S. M. Montgomery, X. Kuang, C. D. Armstrong, and H. J. Qi, "Recent advances in additive manufacturing of active mechanical metamaterials," *Current Opinion in Solid State and Materials Science*, vol. 24, no. 5, p. 100869, 2020.

[28] W. Zhou, D. Li, and Z. Chen, "The influence of ingredients of silica suspensions and laser exposure on UV curing behavior of aqueous ceramic suspensions in stereolithography," *International Journal of Advanced Manufacturing Technology*, vol. 52, no. 5-8, pp. 575–582, 2011.

[29] A. Sorkin, J. Tan, and C. Wong, "Multi-material modelling for selective laser melting," *Procedia engineering*, vol. 216, pp. 51–57, 2017.

[30] J. Whitehead and H. Lipson, "Inverted multi-material laser sintering," *Additive Manufacturing*, vol. 36, p. 101440, 2020.

[31] S. Maruo, K. Ikuta, and T. Ninagawa, "Multi-polymer microstereolithography for hybrid opto-MEMS," *Proceedings of the IEEE Micro Electro Mechanical Systems (MEMS)*, pp. 151–154, 2001.

[32] H. Kim, J. Choi, and R. Wicker, "Scheduling and process planning for multiple material stereolithography," *Rapid Prototyping Journal*, 2010.

[33] H.-C. Kim, J.-W. Choi, E. MacDonald, and R. Wicker, "Slice overlap-detection algorithm for process planning in multiple-material stereolithography," *The International Journal of Advanced Manufacturing Technology*, vol. 46, no. 9-12, pp. 1161–1170, 2010.

[34] J. W. Choi, H. C. Kim, and R. Wicker, "Multi-material stereolithography," *Journal of Materials Processing Technology*, vol. 211, no. 3, pp. 318–328, 2011.

[35] Q. Wang, J. A. Jackson, Q. Ge, J. B. Hopkins, C. M. Spadaccini, and N. X. Fang, "Lightweight mechanical metamaterials with tunable negative thermal expansion," *Physical review letters*, vol. 117, no. 17, p. 175901, 2016.

[36] K. Kowsari, S. Akbari, D. Wang, N. X. Fang, and Q. Ge, "High-Efficiency High-Resolution Multimaterial Fabrication for Digital Light Processing-Based Three-Dimensional Printing," *3D Printing and Additive Manufacturing*, vol. 5, no. 3, pp. 185–193, 2018.

[37] D. Han, C. Yang, N. X. Fang, and H. Lee, "Rapid multi-material 3D printing with projection micro-stereolithography using dynamic fluidic control," *Additive Manufacturing*, vol. 27, no. March, pp. 606–615, 2019.

[38] G. Lipkowitz, T. Samuelsen, K. Hsiao, B. Lee, M. T. Dulay, I. Coates, H. Lin, W. Pan, G. Toth, L. Tate, *et al.*, "Injection continuous liquid interface production of 3d objects," *Science Advances*, vol. 8, no. 39, p. eabq3917, 2022.

[39] B. Adzima, "The Ember Printer: An Open Platform for Software, Hardware, and Materials Development.," in *Uv. eb West Conference.*, 2015.

[40] D. Shah, J. Morris, C. Hansen, and A. Amirkhizi, "DLP-based 3D printing of low-density composite formulations for unit cells for mechanical metamaterials," *Proceedings of the American Society for Composites - 34th Technical Conference, ASC 2019*, 2019.

[41] D. M. Shah, J. Morris, T. A. Plaisted, A. V. Amirkhizi, and C. J. Hansen, "Highly filled resins for DLP-based printing of low density, high modulus materials," *Additive Manufacturing*, vol. 37, no. November 2020, p. 101736, 2020.

[42] J. Morris and A. V. Amirkhizi, "Multi-point scattering measurements for effective property extraction from metamaterials with skin effects," *arXiv preprint arXiv:2206.12453*, 2022.

[43] J. Morris, *Design, Characterization, and Analysis Methods for Low Frequency Mechanical Metamaterials*. PhD thesis, University of Massachusetts Lowell, 2022.

[44] E. Viscione, D. Shah, and C. Hansen, "Modified firmware for mm-dlp ember 3d printer: https://github.com/hansen-research-group/hansen-lab," 2022.

[45] S. P. Gentry and J. W. Halloran, "Depth and width of cured lines in photopolymerizable ceramic suspensions," *Journal of the European Ceramic Society*, vol. 33, no. 10, pp. 1981–1988, 2013.

[46] K. Sekmen, T. Rehbein, M. Johlitz, A. Lion, and A. Constantinescu, "Thermal analysis and shrinkage characterization of the photopolymers for dlp additive manufacturing processes," *Continuum Mechanics and Thermodynamics*, pp. 1–18, 2022.

Supplementary Information

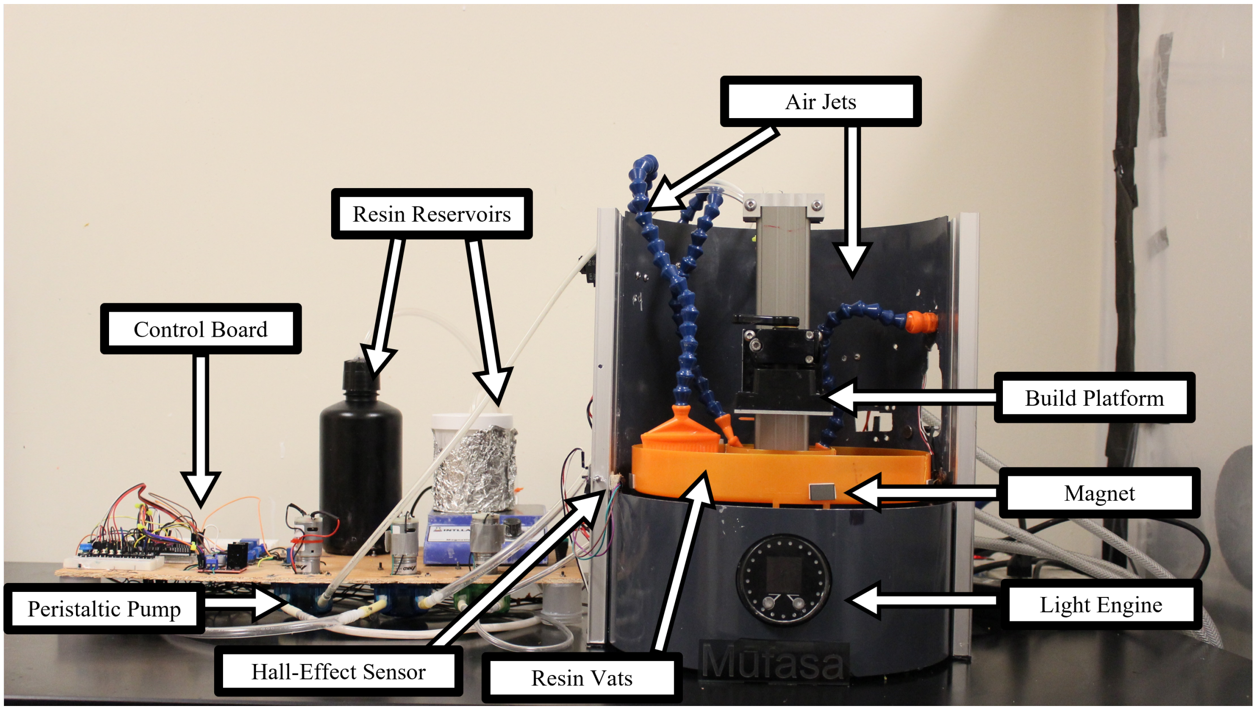

(a)

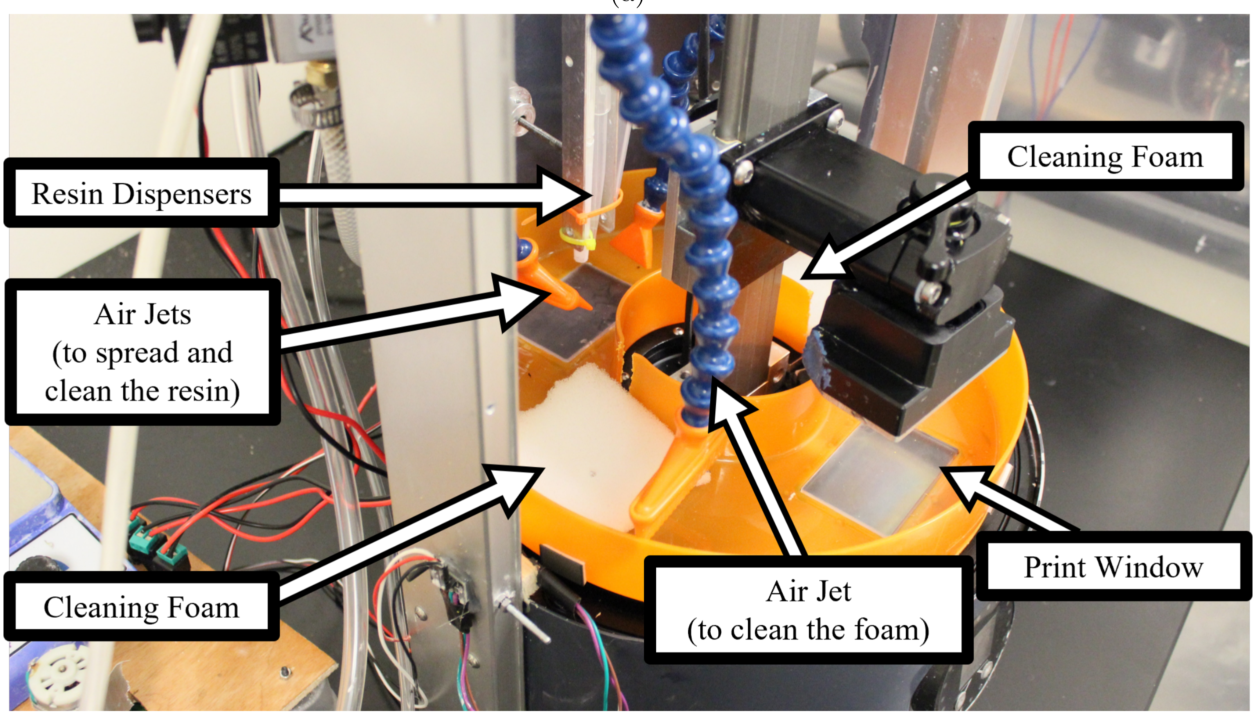

(b)

Figure S.1: a) MM-DLP 3D printer set-up with the external control board. b) MM-DLP resin vats with annotated features.

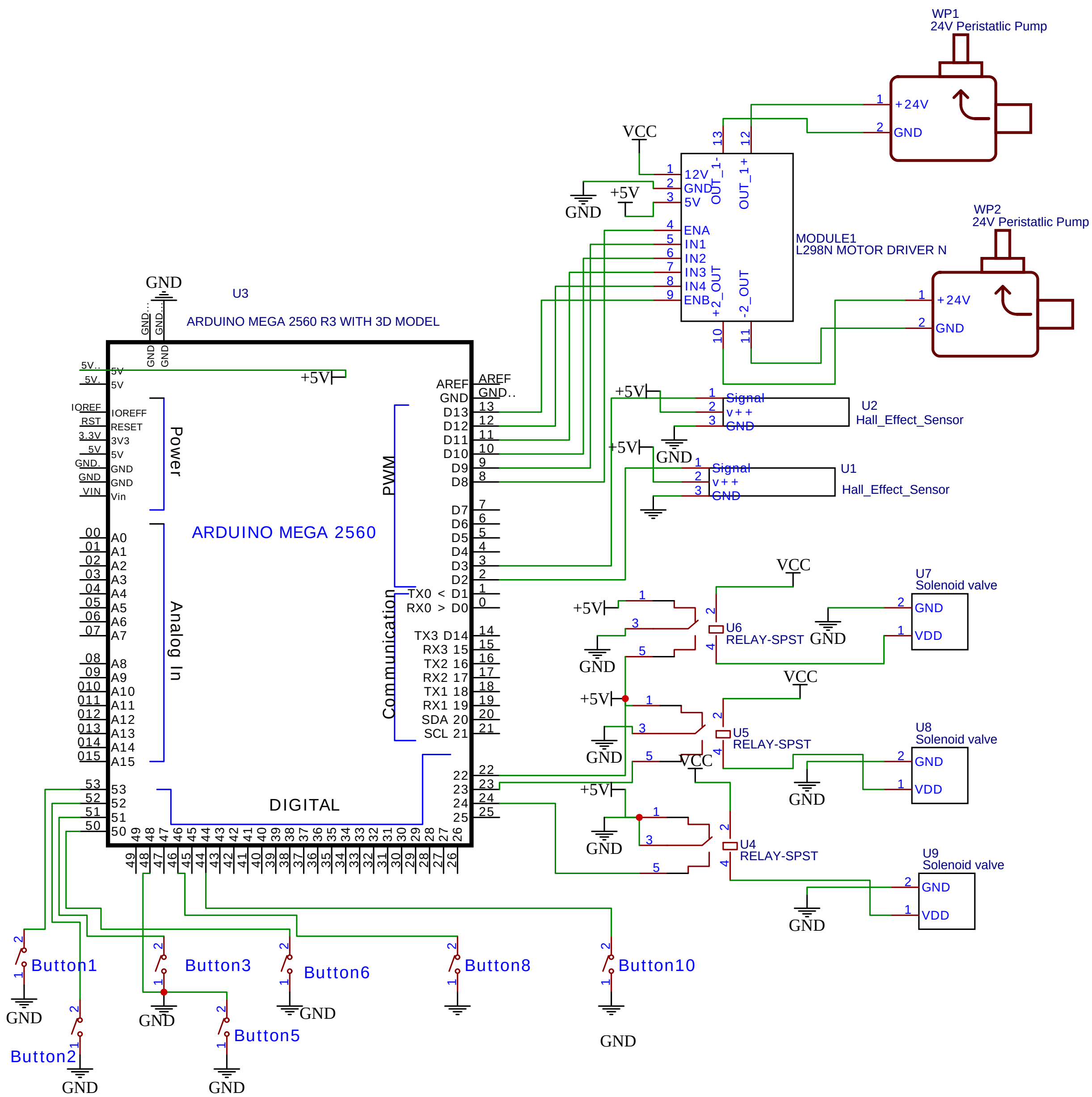

Figure S.2: Control board schematic diagram for the MM-DLP.

The control board for the resin displacement, and cleaning for the MM-DLP 3D printer is built on the Arduino Mega 2560 microcontroller. The Hall-effect sensors pick up the magnetic fields from the magnets placed on the outer walls of the resin trays. The Hall-effect sensor then triggers the microcontroller to perform a programmed action based on the sequence of magnets. The peristaltic pumps are controlled separately through a l298N H-bridge motor controller. The solenoid valves control the release of pressurized air at specified points for cleaning of areas of the print. These valves are actuated with relays connected to the microcontroller. The buttons shown at the bottom of the page are programmed to allow modification of print behavior. Button 1 pauses the microcontroller detection temporarily.

Buttons 2 and 3 reverses the flow of the pumps to clear the system at the end of a print. Button 4 will reset the control system to its initial state. The rest of the buttons are for various debugging and testing purposes.